Molecular Therapy
Nucleic Acids
Original Article

Doxorubicin-Conjugated Innovative 16-mer DNA Aptamer-Based Annexin A1 Targeted Anti-Cancer Drug Delivery

Rohit Bavi,[1,2,10] Zhang Hang,[1,10] Parikshit Banerjee,[3] Md Aquib,[4] Mahendra Jadhao,[5,6] Niraj Rane,[7,8] Sneha Bavi,[9] Raghunath Bhosale,[2] Kisan Kodam,[7] Byong-Hun Jeon,[8] and Yueqing Gu[1]

[1]State Key Laboratory of Natural Medicines, Department of Biomedical Engineering, School of Engineering, China Pharmaceutical University, 24 Tongjia Xiang, Nanjing, Gulou District 210009, China; [2]School of Chemical Sciences, Punyashlok Ahilyadevi Holkar Solapur University, Solapur 413255, Maharashtra, India; [3]School of Pharmacy, Faculty of Medicine, The Chinese University of Hong Kong, Shatin, Hong Kong, China; [4]Department of Pharmaceutics, School of Pharmacy, China Pharmaceutical University, Nanjing, Jiangsu 211198, China; [5]Department of Medicinal and Applied Chemistry, Kaohsiung Medical University, Kaohsiung 80708, Taiwan; [6]Department of Biotechnology, Kaohsiung Medical University, Kaohsiung 80708, Taiwan; [7]Biochemistry Division, Department of Chemistry, Savitribai Phule Pune University, Pune 411007, Maharashtra, India; [8]Department of Earth Resources and Environmental Engineering, Hanyang University, Seoul 04763, Republic of Korea; [9]Axiom Market Research and Consulting, Pune 411014, Maharashtra, India

Aptamers are small, functional single-stranded DNA or RNA oligonucleotides that bind to their targets with high affinity and specificity. Experimentally, aptamers are selected by the systematic evolution of ligands by exponential enrichment (SELEX) method. Here, we have used rational drug designing and bioinformatics methods to design the aptamers, which involves three different steps. First, finding a probable aptamer-binding site, and second, designing the recognition and structural parts of the aptamers by generating a virtual library of sequences, selection of specific sequence via molecular docking, molecular dynamics (MD) simulation, binding energy calculations, and finally evaluating the experimental affinity. Following this strategy, a 16-mer DNA aptamer was designed for Annexin A1 (ANXA1). In a direct binding assay, DNA1 aptamer bound to the ANXA1 with dissociation constants value of 83 nM. Flow cytometry and fluorescence microscopy results also showed that DNA1 aptamer binds specifically to A549, HepG2, U-87 MG cancer cells that overexpress ANXA1 protein, but not to MCF7 and L-02, which are ANXA1 negative cells. We further developed a novel system by conjugating DNA1 aptamer with doxorubicin and its efficacy was studied by cellular uptake and cell viability assay. Also, anti-tumor analysis showed that conjugation of doxorubicin with aptamer significantly enhances targeted therapy against tumors while minimizing overall adverse effects on mice health.

INTRODUCTION

Annexin A1 (ANXA1) is the first member of the annexin superfamily including 12 other members. Structurally, ANXA1 is constituted by a conserved core sequence that has binding properties for calcium and phospholipids, and, functionally, it has ability to bind negatively charged phospholipids in a calcium-dependent manner. Its distinctive N-terminal sequence gives different annexins their functions.[1] Initially, it was discovered to intercede the anti-inflammatory effect of glucocorticoids by inhibiting the phospholipase A2, preventing the arachidonic acid supply needed for prostaglandin synthesis, thus suppressing inflammation.[2] Furthermore, it was also involved in vascular endothelial growth factor-mediated angiogenesis.[3] Although initially ANXA1 was discovered for its role in inflammation, later on it was found to take part in a broad range of molecular and cellular processes, such as cell proliferation, differentiation, apoptosis, regulation of cell migration, and invasion; all of which have implications in the progress and development of cancer.[4]

An increasing number of studies have suggested that ANXA1 is either down-regulated or upregulated in different cancers, so its role may be cancer specific. For instance, in cholangiocarcinoma, ANXA1 is used as a new immunohistological marker, which distinguishes it from pancreatic ductal carcinoma.[5,6] Similarly, to diagnose hairy cell leukemia using immunohistochemistry, ANXA1 is used as a clinical biomarker and also helps in differentiating ANXA1$^+$ hairy cell leukemia from splenic lymphoma with villous lymphocytes and variant hairy cell leukemia.[7] Paraffin-embedded immuno-histochemical staining of primary tumors showed upregulation of ANXA1 in gastric cancer,[8–10] hepatocellular carcinoma,[11] lung adenocarcinoma,[12] melanoma,[13] and pancreatic cancer.[14] This was associated with poor prognosis,[9,11,12] abridged metastasis-free survival,[11] and abridged

Received 13 February 2020; accepted 27 July 2020;
https://doi.org/10.1016/j.omtn.2020.07.038.

[10]These authors contributed equally to this work.

Correspondence: Byong-Hun Jeon, Department of Earth Resources and Environmental Engineering, Hanyang University, Seoul 04763, Republic of Korea.
E-mail: bhjeon@hanyang.ac.kr
Correspondence: Yueqing Gu, State Key Laboratory of Natural Medicines, Department of Biomedical Engineering, School of Engineering, China Pharmaceutical University, 24 Tongjia Xiang, Nanjing, Gulou District 210009, China.
E-mail: guengineering@cpu.edu.cn

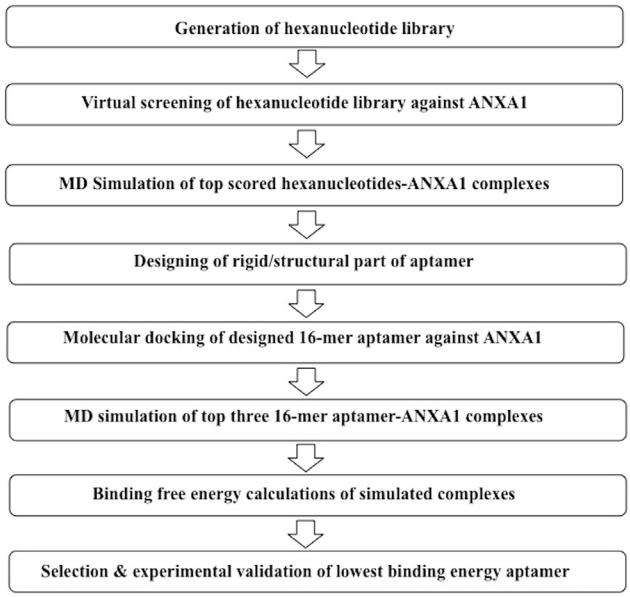

Figure 1. Schematic Workflow of *In Silico* Methodology Used for Identifying Aptamer against ANXA1 Protein

disease-free survival.[9,12] Similarly, low expression of ANXA1 was observed in esophageal carcinoma,[15] head and neck squamous cell carcinoma,[16] prostate carcinoma,[15,17] and nasopharyngeal carcinoma,[18] correlating with differentiation grade.[18,19] This differential expression of ANXA1 may suggest different ways of cancer progression, and its different sub-cellular localizations may determine its functions.

ANXA1 is expressed in the tumor vasculature of all types of tumors in mice and humans,[20] which can be used as a therapeutic biomarker for tumor vasculature-targeting vehicles. Hatakeyama et al.[21] used peptide displaying phage technique to develop a carbohydrate mimetic peptide (IFLLWQR), which specifically binds to ANXA1 with high affinity. However, this peptide displayed poor stability *in vivo*, as it was prone to proteolysis. Therefore, a smaller, efficient, more stable and specific ANXA1 binding ligand is essential for cancer diagnosis and therapy.

Currently, aptamers, a new class of nucleic acid probes, have gained significant attention as molecular probes in biomedical applications. Aptamers are small, functional single-stranded DNA or RNA oligonucleotides with unique three-dimensional structure that binds to their targets with high affinity and specificity. Recently over the past, aptamers were generated for wide variety of targets including co-factors, proteins, inorganic materials, cells, small molecules, viruses, and whole organisms.[22,23] The salient features that make aptamers a promising choice over usual antibodies are that they are less toxic, easily reproducible, low immunogenicity, high stability, fast tissue penetration, and has low molecular weight.[24] Aptamers are selected *in vitro* by the systematic evolution of ligands by exponential enrichment (SELEX) method, which involves screening of large random pool of oligonucleotide sequence libraries by an iterative process of *in vitro* selection and amplification.[25] The entire SELEX method is monotonous, time-consuming without any guarantee of success, and is often compromised by unspecific binding of the oligonucleotides. Moreover, a fixed priming site is required in the combinatorial libraries of oligonucleotides sequences by imposing the size criteria on the random region, consequently hindering the diversity of the synthesized aptamer library.[26]

Hence to overcome these drawbacks, rational drug designing and bioinformatics methods were used to design the aptamers that particularly have high affinity toward a specific protein.[27,28] Here, we have developed the *in silico* method for the development of aptamer by the generation of a virtual library of sequences, selection of specific aptamers via molecular docking, molecular dynamics (MD) simulation, and binding free energy calculations as shown in Figure 1.[28] Microscale thermophoresis (MST) analysis revealed the dissociation constant value of 83 nM between aptamer and ANXA1 protein. Furthermore, the affinity and specificity of DNA1 aptamer was also confirmed by testing it against ANXA1 expressing cancer cell lines. Additionally, we prepared the DNA1 aptamer-doxorubicin conjugate and incubated with ANXA1 expressing cancer cells, which resulted in high concentration and prolonged retention of DOX in the nuclei. Our data demonstrate that free DOX is quickly effluxed through random diffusion after entering cells, whereas DOX released through DNA1 aptamer can evade the drug efflux systems in malignant cells. This novel strategy of drug-delivery system could reduce the tumor chemoresistance toward DOX, thereby improving its therapeutic efficacy.

RESULTS

This work used a Python script (see Supplemental Information) to generate a library of 4,096 possible hexanucleotide structures that were subjected to energy minimization by a CHARMm force field. Data scrapping was done using the Beautiful Soup approach and was programmed to automate the request for all probable combinations of A, T, G, and C nucleotide sequences.

Virtual Screening of a Hexanucleotide Library to Identify the Probable Recognition Part of the Aptamer

The proposed procedure requires the selection of a probable aptamer-binding site. A visual inspection of the human ANXA1 protein structure[29] revealed a positive potential cavity on the surface of the protein. Nevertheless, a hexanucleotide library containing all possible 4,096 combinations was docked on the entire surface of the ANXA1 protein to select the most probable aptamer binding sites. The protein surface (Figure S1A) subsequently showed a possible aptamer-binding site that accommodated roughly 95% of the docked poses. The remaining 5% of the hexanucleotides were found on the opposite axial side of the aptamer-binding site and were redocked into the possible binding site (Figure S1B). The best-docked conformations were selected based on the binding free energy. The best value for the Autodock scoring function was found for the 5′-AATGGG-3′ oligonucleotide with

−12.9 kcal/mol while 5′-CTGGCA-3′ showed a low value of −7.0 kcal/mol. Here, strong binding energy (negative sign) specifies a higher binding affinity of oligonucleotide with proteins via stable intermolecular interactions.

MD Simulations and Binding Free Energy Calculations of Hexanucleotide Protein Complex

We next further optimized and evaluated the dynamic binding behavior of the selected hexanucleotide with the ANXA1 protein via MD simulations. The dynamic binding behavior of the protein hexanucleotide complex during 20 ns of simulation was studied by computing the backbone root mean square deviation (RMSD) of the protein, hexanucleotide, potential energy of the system, and intermolecular hydrogen bonds (Figure S2). The backbone RMSD plots of the protein and hexanucleotide are plotted as a function of time. The RMSD values for the protein were between 0.10 nm and 0.18 nm throughout their simulations except for the protein interacting with 5′-GGGGGA-3′ hexanucleotide, which showed a maximum deviation between 5 ns and 10 ns. Later, it achieved a plateau (Figure S2A). The protein structures were stable and well relaxed over the simulation period. The RMSD values for hexanucleotides were stable and converged over the simulation time apart from AATAAA, which rapidly increased after 13 ns and deviated from 0.4 nm and 0.55 nm (Figure S2B). The RMSD values for the other hexanucleotides were between 0.23 nm and 0.37 nm, indicating that the majority of complexes had an optimal conformation throughout the simulation time. The system's potential energy was stable over the simulation time, signifying that no abnormal behavior occurred in the complex during the simulation as shown in Figure S2C. To understand the binding mode, we monitored the intermolecular hydrogen bonds between hexanucleotide and protein during the simulation period as shown in Figure S2D. The average numbers of hydrogen bonds between protein and hexanucleotides were 9, 4, 9, and 8 for 5′-AATGGG-3′, 5′-AATAAA-3′, 5′-GGGGGA-3′, and 5′-TGACTC-3′, respectively. 5′-AATAAA-3′ showed relatively fewer hydrogen bonds compared to the others. The average number of hydrogen bonds shows their key role in providing stability to the complex.

The binding free energy calculation study was useful in calculating the binding potential of hexanucleotides because it offers a quantitative estimation of the binding free energy.[30–34] The MM-PBSA method was used to calculate the binding free energy of the selected hexanucleotides to their protein. The calculations were performed by extracting the trajectories from the last 5 ns when the system was well-equilibrated. The MM-PBSA calculation gave favorable ΔG values in the range of 200 kJ/mol to −750 kJ/mol as shown in Figure S3. The energy fluctuation in each snapshot may be because the conformational space was not sampled enough to get converged results. The average binding energy obtained for protein-hexanucleotide complexes was −309.0 kJ/mol (5′-AATGGG-3′), −147.76 kJ/mol (5′-AATAAA-3′), −115.19 (5′-GGGGGA-3′), −141.26 (5′-TGACTC-3′), and −92.38 (5′-AGGGAC-3′) as shown in Figure S3. The MM-PBSA method predicted stronger binding interaction for 5′-AATGGG-3′ than the other hexanucleotides and is in line with the docking results. Thus, docking, MD simulation, and binding free energy calculation results suggest that most of the hexanucleotides interact but 5′-AATGGG-3′ has a stronger binding affinity with the selected binding site on the surface of the protein.

Designing the Rigid/Structural Part of Aptamer

In this step, the structural part of the aptamer was designed by elongating the hexanucleotide on either side by the complementary base. This structural part of the aptamer will help in maintaining the optimal binding conformation of the recognition part of the aptamer. Electrostatic potential distribution and visual inspection of the hexanucleotide-binding site revealed that the elongation of the hexanucleotide on either site would not hinder binding of the protein. The hexanucleotides were extended by adding 5′-GCGCG-3′ sequence at the 5′ end and its complement sequence 5′-CGCGC-3′ at the 3′ end, which resulted in a hairpin-like structure. Thus, the fusion of the structural (5′-GCGCG-3′ and 5′-CGCGC-3′) and recognition (5′-XXXXXX-3′) parts generated the full aptamers having the sequence 5′-GCGCGXXXXXXCGCGC-3′. The recognition parts used were the top three hexanucleotide (5′-AATGGG-3′, 5′-AATAAA-3′, 5′-GGGGGA-3′) sequences obtained from the modeling studies. In further studies, aptamers having the sequence 5′-GCGCGAATGGGCGCGC-3′, 5′-GCGCGAATAAACGCGC-3′, and 5′-GCGCGGGGGGACGCGC-3′ will be referred to as DNA1, DNA2, and DNA3, respectively. The secondary structure prediction and the best-docked pose of DNA1 having the highest binding affinity are shown in Figures 2A and 2B, respectively.

MD Simulation and Interaction Energy Calculations of Aptamer Protein Complex

The aptamers were docked on the preferred binding site to check the feasibility of all the designed 16-mer aptamers to interact with the selected binding site of the protein. During molecular docking, the recognition part of the aptamer was kept flexible while the structural part of the aptamer was kept rigid. The 16-mer aptamers were docked successfully with good overlapping and are shown in Figure 2C. Docking results are tabulated in Table S1. The dynamic binding behavior of the docked complex was further studied by subjecting it to MD simulation. The binding behavior of the aptamer-protein complex was calculated by plotting the geometrical features such as RMSD, intermolecular hydrogen bonds, and interaction energy as a function of time; the resulting graphs are shown in Figure S4.

Next, we calculated the backbone RMSD for the protein and DNA aptamer to determine the structural deviation from the initial structure. The RMSD plot for the protein in complex with DNA2 and DNA3 showed relatively fewer structural deviations compared to the initial structure throughout the simulation time with an average RMSD of 0.15 nm and 0.17 nm, respectively, as revealed in Figure S4A. This trend was not observed in the case of protein in complex with DNA1 because it showed a higher conformational flexibility after 20 ns with a maximum RMSD of 0.25 nm (Figure S4A). The RMSD values for the 16-mer DNA aptamer in protein-DNA1 and protein-DNA2 complex showed relatively fewer structural

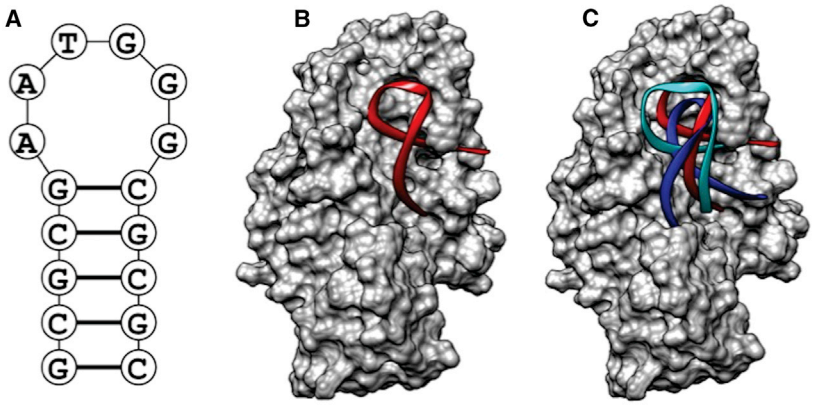

Figure 2. Molecular Docking and Dynamic Simulation of Aptamer

(A) The predicted 2D structure of DNA1 aptamer by RNAfold. (B) The bound conformation of DNA1 aptamer to ANXA1. (C) The binding mode of DNA1 (red), DNA2 (blue), and DNA3 (cyan) in the binding site of ANXA1 protein. DNA molecules in their representative structures are superimposed.

fluctuations with respect to protein-DNA3 complex. The 16-mer DNA3 aptamer showed a regular structural deviation from the initial structure throughout the simulation period (Figure S4B). Such fluctuations may be due to the optimization of interactions with the protein structure, as well as with the surrounding water molecules. The average RMSD values for DNA1, DNA2, and DNA3 are 0.30 nm, 0.31 nm, and 0.33 nm, respectively. The intermolecular hydrogen bonds were also calculated between protein atoms and their respective DNA aptamer and were plotted as a function of time (Figure S4C). On average, DNA1, DNA2, and DNA3 formed 11, 7, and 6 hydrogen bonds, respectively, with the respective protein. Unlike DNA2 and DNA3 aptamers, DNA1 formed the highest number of intermolecular hydrogen bond contacts with the protein after 20,000 ps. This may be due to the conformational change in protein and DNA1, which led to favorable interactions between them.

The average non-bonded interaction energy (E^{inti}) provides an approximation for gauging the binding affinity and was also calculated for all frames in MD simulation trajectories. The E^{inti} values were calculated specifically between proteins and their aptamers and were found to be highly favorable for the DNA1 and DNA2 aptamers and least favorable for the DNA3 aptamer (Figure S4D). The favorable interaction energies (Kcal/mol) were on the order of DNA1 (−1,200) > DNA2 (−600) > DNA3 (−450). Further analysis showed that a major contribution to overall non-bonded interaction energy, E^{int}, comes from the Coul term while the remaining comes from the LJ term. The molecular modeling studies show that the DNA1 aptamer has a stronger binding affinity with the selected binding site on the surface of the ANXA1 protein and were further subjected to experimental analysis.

Analysis of Binding Interactions between hANXA1 Protein and DNA1 Aptamers via MST

MST detected a direct interaction between purified, soluble Histidine (His)-tagged hANXA1 protein labeled with Red-tris-NTA dye and the DNA1 aptamer. The K_D (dissociation constant) value of 83 ± 4 nM was observed with the aptamer and hANXA1 protein as shown in Figure S5. A lower K_d value suggested a strong affinity of the aptamer to the hANXA1 protein.

Evaluating Binding Specificity of the Aptamers by Flow Cytometry Assays

To confirm the specificity of the designed DNA1 aptamers, we tested a FAM-labeled aptamer against various ANXA1-expressing cancer cell lines including A549, HepG2, and U-87 MG as positive cell lines, and MCF7 and L-02 as negative cell lines. FAM-labeled IF7 peptide is selectively known to bind ANXA1 and was chosen as a positive

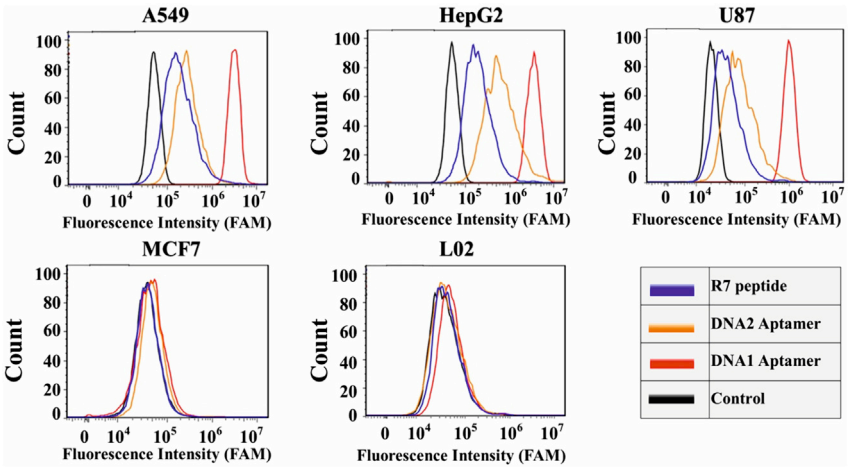

Figure 3. Flow Cytometric Analysis of DNA1, DNA2 Aptamer with A549, HepG2, U87 MG, L02, and MCF7 Cells

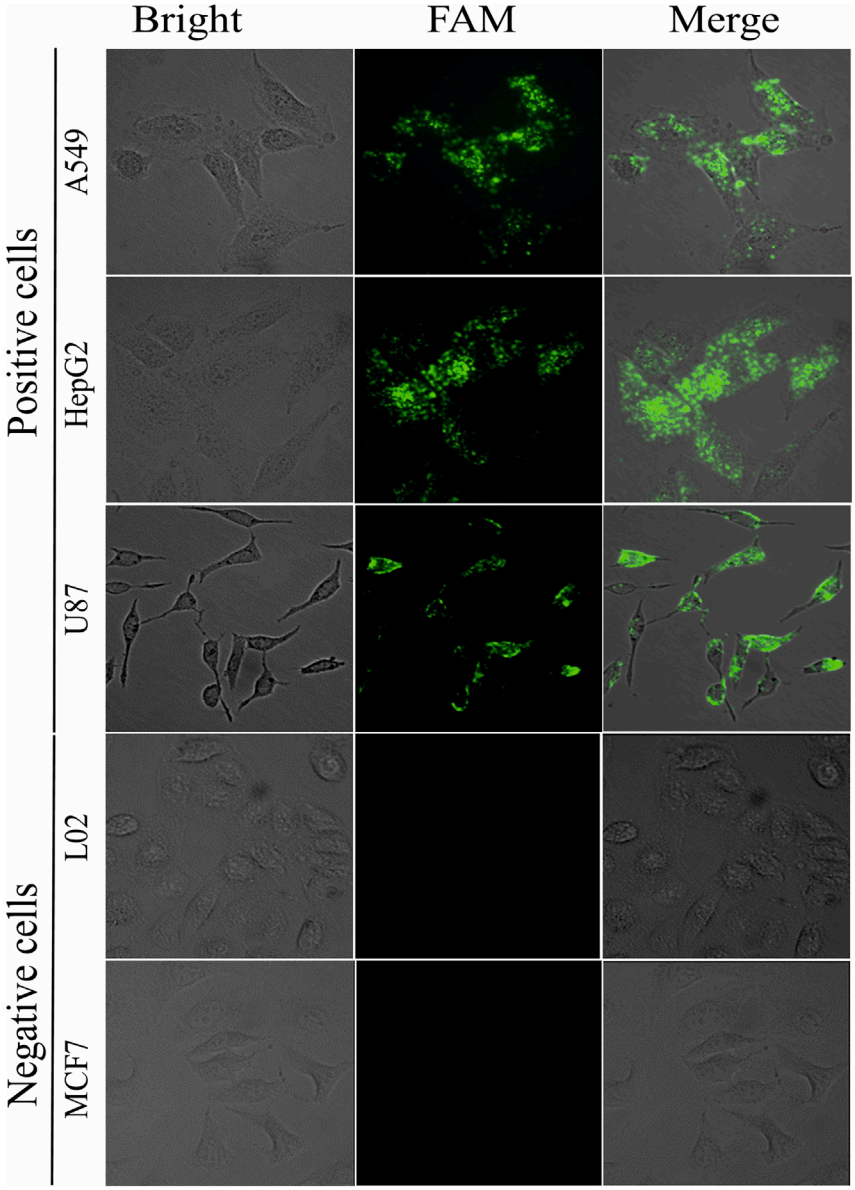

Figure 4. Subcellular Distribution Analysis of DNA1, DNA2 Aptamer with A549, HepG2, U87 MG, L02, and MCF7 Cells
Scale bars, 20 μm.

control. The interactions of DNA1, DNA2 aptamer, and IF7 peptide with different cancer cell lines were examined by flow cytometry. Figure 3 shows that DNA1, DNA2 aptamer, and IF7 peptide displayed a shift in fluorescence intensity indicating a strong binding interaction toward A549, HepG2, and U-87 MG while no significant recognition was observed toward L-02 and MCF7 cells signifying their exceptional specificity. The DNA1 aptamer showed a higher fluorescence intensity then DNA2 aptamer and IF7 peptide indicating higher affinity.

Fluorescence Microscopy Imaging of Cells with Aptamers

Live cell fluorescence microscopic imaging was performed to verify the interaction between DNA1 aptamer and ANXA1-expressing cancer cell lines. High-fluorescence signals were shown for A549, HepG2, and U-87 MG cells while no fluorescence signals were observed for L-02 and MCF7 cells when incubated with the FAM-labeled DNA1 aptamer (Figure 4). Thus, the DNA1 aptamer could differentiate between ANXA1-positive and -negative cells.

Evaluating the Binding Specificity of DNA1 Aptamer in ANXA1 Knockdown HepG2 and A549 Cells

To validate the specific binding of the DNA1 aptamer to ANXA1, we performed ANXA1 gene silencing in ANXA1-expressing HepG2 and A549 cells. ANXA1 small interfering RNA (siRNA) transfection significantly lowered ANXA1 mRNA levels in both HepG2 and A549 resulting in low protein expression (Figure 5, left panel). Figure 5 (right panel) shows a relatively smaller shift in fluorescence intensity in siRNA-treated cells compared to non-treated and control siRNA-treated cells indicating low binding affinity. Thus, DNA1 aptamer shows a strong and specific binding affinity toward ANXA1-expressing HepG2 and A549 cells compared to ANXA1-deficient L-02 and MCF7 cells.

Evaluation and pH-Dependent Release of DOX from DNA1 Aptamer

It is well known that DOX can intercalate within the aromatic rings of 5′-CG-3′ or 5′-GC-3′ in double-stranded DNA.[35] A secondary structure prediction tool called Nucleic Acid Package (NUPACK)[36] showed four possible DOX binding sites on the duplex region of the DNA1 aptamer. The DOX loading capacity of the DNA1 aptamer was studied by monitoring the quenching of its natural fluorescence emission upon intercalation. The optimal molar ratio of doxorubicin loading into the DNA1 aptamer was 0.4, which resulted in quenching of the DOX fluorescence reaching a plateau of approximately 79% (Figure 6A). Figure 6B shows that after 10 h, around 31% of DOX was released from DNA1 aptamer-DOX conjugate in a PBS buffer having a pH of 7.4 signifying excellent stability of the DNA1-Aptamer-DOX conjugate under functional pH when transiting in the blood. We next estimated the pH-dependent release of DOX from the DNA1 aptamer at different pH levels at room temperature. Figure 6C shows that an initial spurt of DOX release was observed at acidic pH shadowed by a stable and constant release at pH 5.0 with over 70% of DOX released

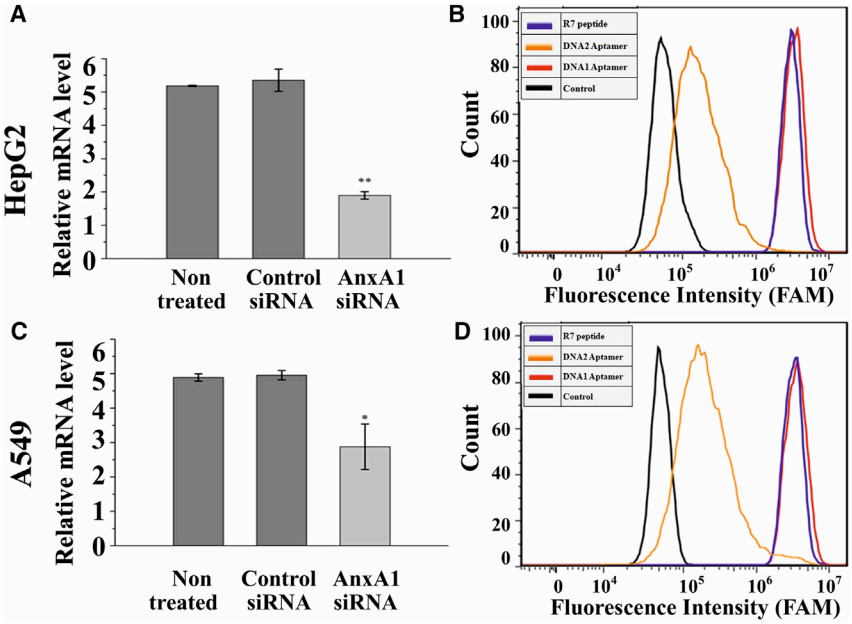

Figure 5. Establishment of ANXA1 Gene Knockdown Cells and Functional Analysis of DNA1 Binding Specificity by Flow Cytometry

(A) mRNA levels of ANXA1 in HepG2 cells after control and ANXA1 siRNA treatment. (B) Quantitative results of flow-cytometric analysis of DNA1 binding specificity in control and ANXA1 knockdown HepG2 cells. (C) mRNA levels of ANXA1 in A549 cells after control and ANXA1 siRNA treatment. (D) Quantitative results of flow-cytometric analysis of DNA1 binding specificity in control and ANXA1 knockdown A549 cells. $^{**}p < 0.001$, $^{*}p < 0.01$.

after 48 h. Meanwhile, DNA1 aptamer conjugated DOX showed 41% and 30% release after 48 h at pH 7.4 and pH 8.0, respectively. The drug should be released in a pH-dependent manner because it can reduce the systemic exposure of DOX to sensitive organs under functional environments (pH 7.4), but this permits rapid release of DOX from the aptamer-DOX complex after endocytosis.

Evaluation of the Cytotoxic Potential of Drug-Aptamer Conjugate

A 3-(4, 5-dimethylthiazol-2-yl)-2, 5-diphenyltetrazolium bromide (MTT) assay was performed to evaluate the cytotoxicity of DNA1 aptamer, DNA1-DOX conjugate, and free DOX. A dose-response curve was recorded in A549 cell lines after 24 h of treatment. Free DOX showed 26% cell viability, whereas DNA1 and DNA1-DOX conjugate showed 81% and 34% viability at 24 h (Figure 7B). The 50% inhibitory concentrations (IC_{50}) value of free DOX, DNA1, and DNA1-D0X conjugate was 3.162 μg/mL, 4.192 μg/mL, and 3.287 μg/mL, respectively, as shown in Figure 7A. Whereas, in MCF cells free DOX, DNA1, and DOX-DNA1 group showed 24%, 91%, and 60% viability, respectively (Figure 7D). IC_{50} value of formulation groups in MCF7 cells was also found to be 3.205 μg/mL, 5.181 μg/mL, and 4.655 μg/mL, for free-DOX, DNA1, and DOX-DNA1 group, respectively (Figure 7C).

Obtained data showed a dose-dependent cell cytotoxicity with increasing drug concentration that significantly lowered viability of A549 and MCF7 cells. The DNA1 aptamer is almost ineffective in killing cancer cells compared to free DOX and DNA1-DOX conjugate. As in the uptake study, we found higher targeting ability of DNA1-DOX conjugate against cancer cells. Overall, the data confirm that actively targeted DNA1-DOX conjugate can provide significant cytotoxicity against cancer cells while minimizing the non-targeted adverse effects of free DOX. Results also indicated that in ANXA1-positive A549 cells, not much difference in cell viability between free-DOX and DNA1-DOX conjugate has been observed. However, in ANXA1-negative MCF7 cells, cytotoxicity of DNA1-DOX conjugate diminished significantly compared to free DOX. Results revealed that DNA1 aptamers reduced the damage of ANXA1-negative MCF7 cells due to slow release of DOX from the DNA1 aptamer conjugate, while in ANXA1-positive A549 cells DNA1 aptamers supported in retaining the efficacy of DOX by enhancing cytotoxicity of the DNA1-DOX conjugate.[37]

DNA1 Aptamer-Mediated Intracellular Targeting of DOX

CLSM imaging of A549 cell after incubation with free DOX and DNA1 aptamer conjugated DOX was conducted to examine the aptamer-mediated cellular uptake of doxorubicin. Observation after 2 h showed that free DOX readily diffuses through the membranes and reached the nuclei. Also, the DNA1-DOX conjugate was readily internalized by A549 tumor cells with a comparatively stronger fluorescence signal in both nucleus and cytoplasm (Figure 8A). Similarly, after 12 h of incubation, a stronger fluorescence intensity was observed in DNA1-DOX-treated cells versus free DOX as shown in Figure 8B. The uptake mechanism of free DOX and DNA1-DOX is quite different. Free DOX is almost entirely internalized in the nucleus region, whereas DNA1-DOX shows both nucleus and cytoplasmic fluorescence signals.

In Vivo Anti-Tumor Activity of DOX-DNA1 Conjugate in Immunodeficient Mice Model

PBS, free-DOX, DNA1, and DNA1-DOX conjugated were intravenously injected into the 4T1 tumor-bearing mice throughout treatment duration. Tumor volume and body weight were recorded throughout the treatment period as shown in Figures 9A and 9B. The survival of mice was also being monitored closely. The animal body weight changes indicate that similar to the PBS group, the DNA1-DOX conjugate triggered markedly less variation in body weight compared to free DOX and DNA1 aptamer (Figure 9B). Among all the treatment group highest decrease in body weight was observed in free DOX group, indicating severe systemic cytotoxicity of DOX. The DNA1-DOX conjugate significantly decreased

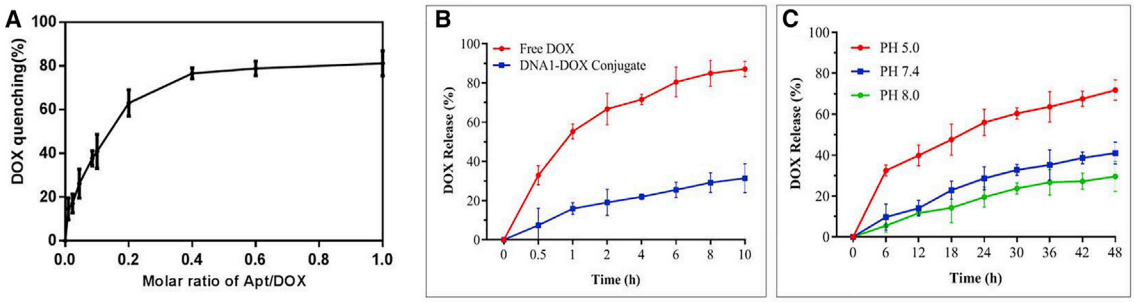

Figure 6. Characterization of ANXA1 Aptamer-DOX Conjugate

(A) The quenching study of DOX after 30 min of incubation with growing concentration of DNA1 aptamer-to-DOX. (B) *In vitro* release of DOX from aptamer in time-dependent manner at pH 7.4. free "DOX" was used to prove the capacity of DOX to dissociate from the DNA1 aptamer and can pass the dialysis membrane. (C) pH-dependent release of DOX from DNA1 aptamer at pH of 5.0, 7.4, and 8.0 respectively.

tumor volume compared to PBS (<0.05). The tumor volume data also revealed that free DOX indeed inhibited the tumor growth, but conjugating DNA1 aptamer with DOX markedly enhanced the suppressive effects of free DOX with DNA1-DOX showing tumor volume noticeably smaller compared to the groups treated with free DOX and DNA1 (Figure 9C). Tumor growth inhibition rate (TIR%) data revealed that delivering DOX conjugated with DNA1 aptamer was significantly (<0.05) more efficacious in inhibiting the tumor growth rate (50.98%) compared to free DOX (35.26%) and DNA1 aptamer (13.16%; Figure 9D). The survival rate was also noticeably higher in the DNA1-DOX conjugate group than in the PBS, DNA1 aptamer, and free DOX groups, respectively as shown in Figure 9E, confirming acceptable safety profile of DOX-DNA1 conjugates *in vivo*.

DISCUSSION

We describe here a new computational methodology for the design of the aptamer. In this method, the aptamer is divided into two parts: the flexible part and the rigid part. The flexible or recognition region of the aptamer is involved in the interaction with the hotspot of the target and, thus, the binding affinity. The rigid or structural region of the aptamer helps to maintain the spatial arrangement of the flexible part. This proposed method involves several computational steps: first, a preferred binding site is searched on the surface of the target protein. It comprises visual inspection of the entire surface of the target protein and also the hexanucleotide docking on the protein structure. In our case, visual inspection showed a positive potential cavity on the surface of the protein that accommodated roughly 95% of the docked poses. The remaining 5% of the hexanucleotide was found on the opposite axial side of the aptamer-binding site and was redocked into the possible binding site in the second step of the aptamer design.

We know that only a few nucleotides of the aptamer directly interact with the target protein while the remaining nucleotides show a temporary interaction with a protein; this was also proven by a long MD simulation.[38] The same mechanism was used to design the recognition part of the aptamer. The next step consists of designing the rigid or structural part of the aptamer whose main function is to maintain the spatial arrangement of the recognition part. A structural difference is observed in the known aptamer, which includes pseudoknots, hairpins, G-quadruplexes, and tetraloops.[39] Here, a double helix was preferred because the hexanucleotide formed a U-like conformation in the binding site of the protein. The hairpin structure was formed after the fusion of the structural and recognition parts of the aptamer.

MD simulation and MM-PBSA results indicate that the designed aptamer can form a stable complex, which was also shown by MST. The DNA1 aptamer accommodated several DOX molecules in the duplex region yielding a therapeutically active complex. The DOX was held in the DNA1 aptamer at a neutral pH and was released at an acidic pH, which is an important criterion for the success of targeted cancer therapy. This result indicates the stable conjugation of DOX with DNA1 aptamer in blood circulation and tissue interstitium, which is released after delivery in the endosome-lysosome compartment. Thus, the cytotoxic effect of DOX is exerted in the target cells to boosting the therapeutic effect of the DNA1 aptamer-DOX conjugate. Confocal microscopy results revealed a higher accumulation of DOX in nuclei via the DNA1 aptamer-DOX conjugate compared to free DOX. These results indicate that free DOX is quickly effluxed through random diffusion after entering cells. In contrast, DOX released through the DNA1 aptamer can evade the drug efflux systems in malignant cells. Similarly, better *in vivo* efficacy of DNA1-DOX conjugated can be attributed to the aptamer-mediated active targeting, as DNA1 aptamer aided the binding of aptamer-drug conjugate to the ANXA1 in cells, thus facilitating the uptake to DOX by target cells *in vivo*.[40] This novel drug-delivery system can reduce the tumor chemo-resistance toward DOX thus improving its therapeutic efficacy.

MATERIALS AND METHODS

A Python script was used to generate the library of 4,096 possible hexanucleotide structures and was minimized by CHARMm force field of Discovery Studio (DS). Data scrapping was done by the beautiful soup approach and was programmed to automate the request for all probable combinations of A, T, G, and C nucleotide sequences.

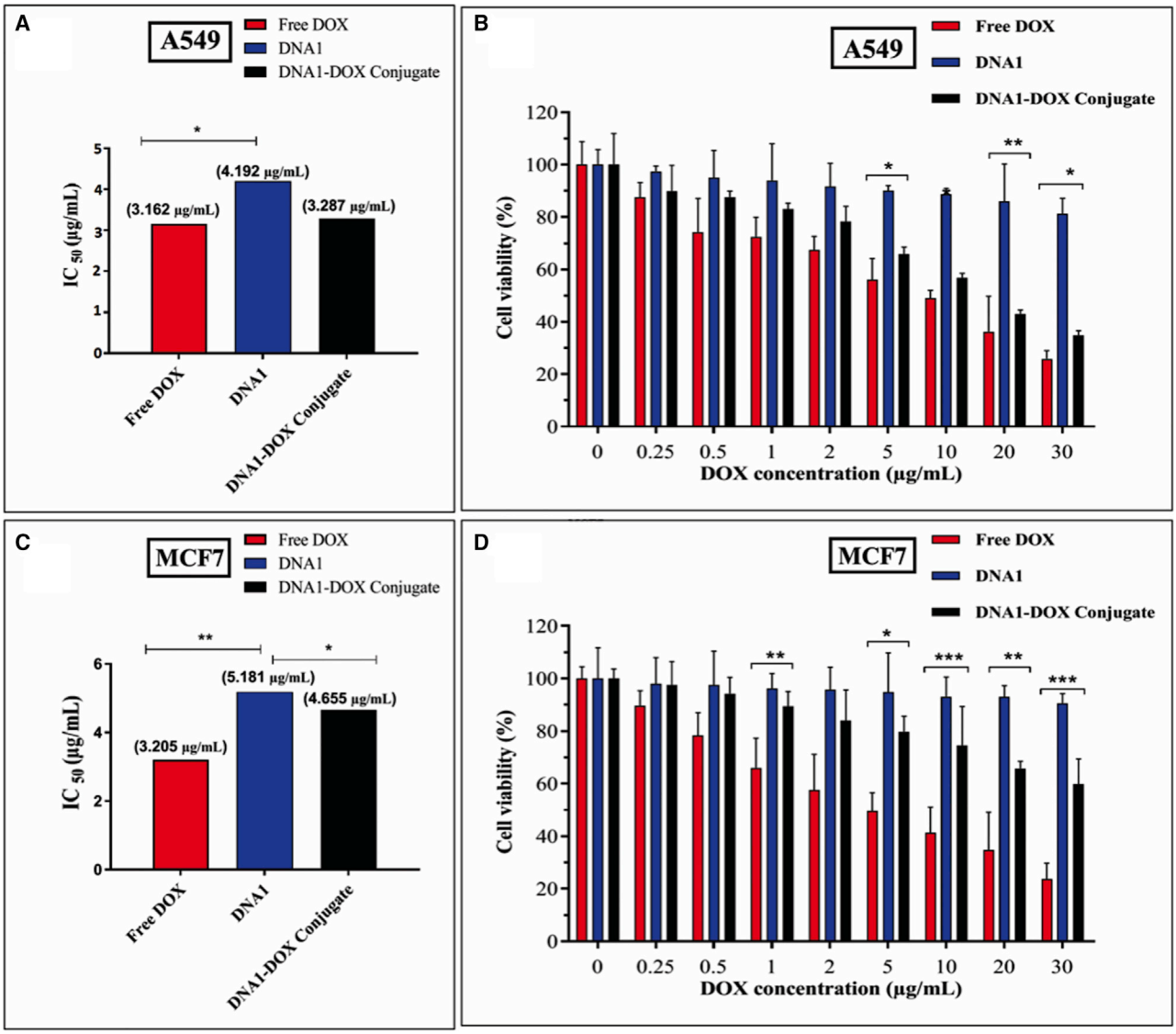

Figure 7. Evaluation of the Cytotoxic Potential of Aptamer-Drug Conjugate

(A) Cytotoxicity of free DOX, DNA1, DNA1-DOX conjugate on the ANXA1-positive A549 cell lines after 24 h. (B) IC_{50} value of different treatment groups in A549 cell lines. (C) Cytotoxicity of free DOX, DNA1, DNA1-DOX conjugate on the ANXA1-negative MCF7 cell lines after 24 h. (D) IC_{50} value of different treatment groups in MCF7 cell lines. *$p < 0.05$, **$p < 0.01$, and ***$p < 0.001$ denotes statistical significance (n = 3, mean ± SD).

Molecular Docking

AutoDock Vina program[41] implemented with MPI was used to screen the entire structure of ANXA1 protein, so as to find the preferred docking sites for each of the hexanucleotides. Python script of AutoDock tools was used to prepare the protein and hexanucleotides files for molecular docking. Prior to docking, the Gasteiger charges and polar hydrogen atoms were added to hexanucleotide and receptor molecule using *OpenBabel*. Keeping the docking parameters to their default values, 50 docking runs were performed, and the results were ranked according to their binding free energies. The best-docked conformation was selected based on the lowest binding free energy with maximum clusters.

MD Simulation

MD simulation was performed to study the dynamic behavior of protein aptamer complex by applying amber99sb-ildn[42] force field implemented in GROMACS 5.0.7 package. Over the recent past, this force field was seen as useful in studying the structure and dynamics of the protein-nucleic acid complex.[43,44] The protein aptamer complex was solvated in the cubic box of TIP3P water model. The negatively charged system was neutralized by adding Na^+ counter-ions. Steepest descent method was used to energy minimize the system, by eliminating the hard contacts from the initial structure until tolerance of 2,500 kJ/mol. In the next step, 500 ps equilibration was done under NVT ensembles by using a V-rescale thermostat at 300 K

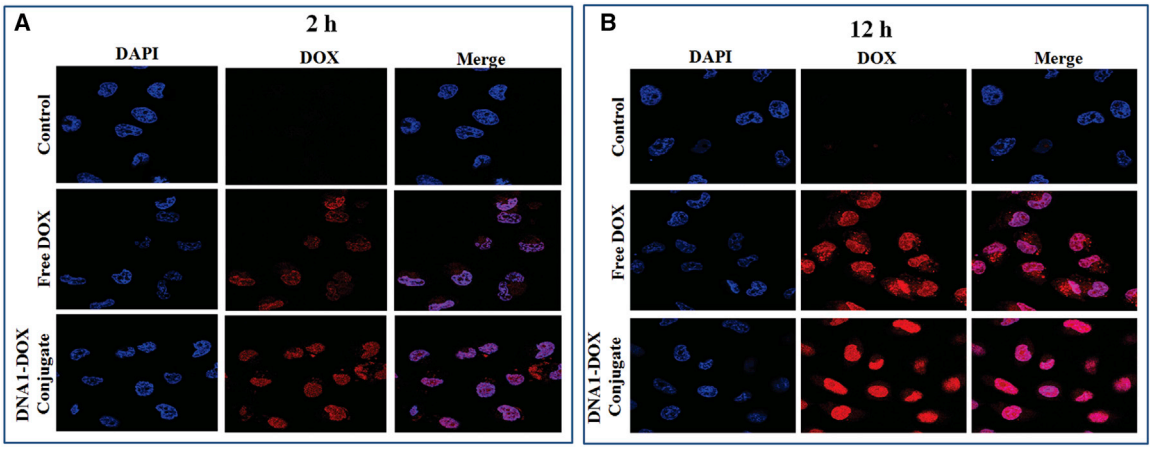

Figure 8. Analysis of Intracellular Uptake of Free DOX and DNA1-DOX Conjugate

(A and B) Confocal imaging microscopy shows the intracellular distribution of free Dox and DNA1-DOX conjugate in A549 cells at (A) 2 h and (B) 12 h. Scale bars, 10 μm.

temperature. The NPT equilibration was performed for 1,000 ps at 1 bar using Parrinello-Rahman barostat. Finally, the equilibrated structures of protein-hexanucleotide complex and protein-aptamer complex from NPT were subjected to 20 ns and 50 ns production run, respectively, at 1 bar pressure and 300 K temperature. The bonds were constrained by applying the LINCS algorithm.[45] The long-range electrostatic interactions were calculated by using the Particle Mesh Ewald (PME) method with a cutoff distance of 1.2 nm.[46] The MD simulations were done in periodic boundary conditions. GROMACS tools, DS, and visual MD (VMD) software were used to analyze the trajectories.

Calculation of Interaction Energies

The strength of the aptamer protein association is quantified by calculating the average non-bonded interaction energies $\langle E^{int} \rangle$ from the total simulation time as per the given equation.

$$E^{int} = \langle LJ \rangle + \langle Coul \rangle$$

Here, $\langle E^{int} \rangle$ represents the average energy in Kcal/mol obtained from the MD simulation. LJ is the short-range Lennarde Jones interaction energy while Coul denotes the Coulomb interaction energy. g_energy tool of gromacs was used to calculate the average short-range LJ and Coul interaction energies between the ANXA1 protein residues and aptamers.

Microscale Thermophoresis Analysis

Recombinant human ANXA1 (hANXA1) protein (Abcam, catalog number ab86466) was procured and labeled with Monolith NT His-Tag labeling kit RED-tris-NTA. The recombinant hANXA1 protein is having a molecular weight of 38.7 kDa. 50 nM protein concentration was used in this assay. The His labeling dye binds efficiently with His-tags, which contains six histidine or more. This dye binds specifically to proteins without an additional step of excess dye removal. High-performance liquid chromatography (HPLC)-purified DNA1 aptamer was procured from Integrated DNA Technologies (USA). The DNA1 aptamer was having 100 μM stock concentration and was further serially diluted to 5μM. The non-labeled aptamer (5 μM) in 10 μL volume was serially diluted 16-fold in Hank's balanced salt solution (HBSS) buffer and then equal amount of 10 μL of 50 nM recombinant hANXA1 protein was added to all the 16 tubes. The samples were then mixed and loaded on glass capillaries and subjected for analysis using Monolith NT.115 of the Nanotemper Technologies (München, Germany). The NT analysis software was used to obtain the values and also to plot the fluorescence signal against the concentration of the ligand with the generation of binding curves revealing the dissociation constant for the interactions. Further, NT analysis software was used to derive the K_d value.

Cell Culture

Human tumor cell lines including adenocarcinoma (A549), hepatocellular carcinoma (HepG2), breast cancer (MCF7), glioblastoma (U-87 MG), and hepatocyte (L-02) were maintained in our laboratory. Dulbecco's modified Eagle's medium supplemented with 10% (v/v) fetal calf serum, 100 U/mL penicillin, and 100 mg/mL streptomycin was used to culture this cell lines and incubated at 37°C in the presence of 5% CO_2 atmosphere. All animal experiments were carried out in compliance with the Animal Management Rules of the Ministry of Health of the People's Republic of China (document no. 55, 2001) and the guidelines for the Care and Use of Laboratory Animals of China Pharmaceutical University. All the animals involved were treated in accordance with protocols evaluated and approved by the Ethical Committee of China Pharmaceutical University.

DNA1 Aptamer

DNA1 aptamer was synthesized and labeled on 5′ end with FAM fluorescent tag by Sangon Biotech (Shanghai, China).

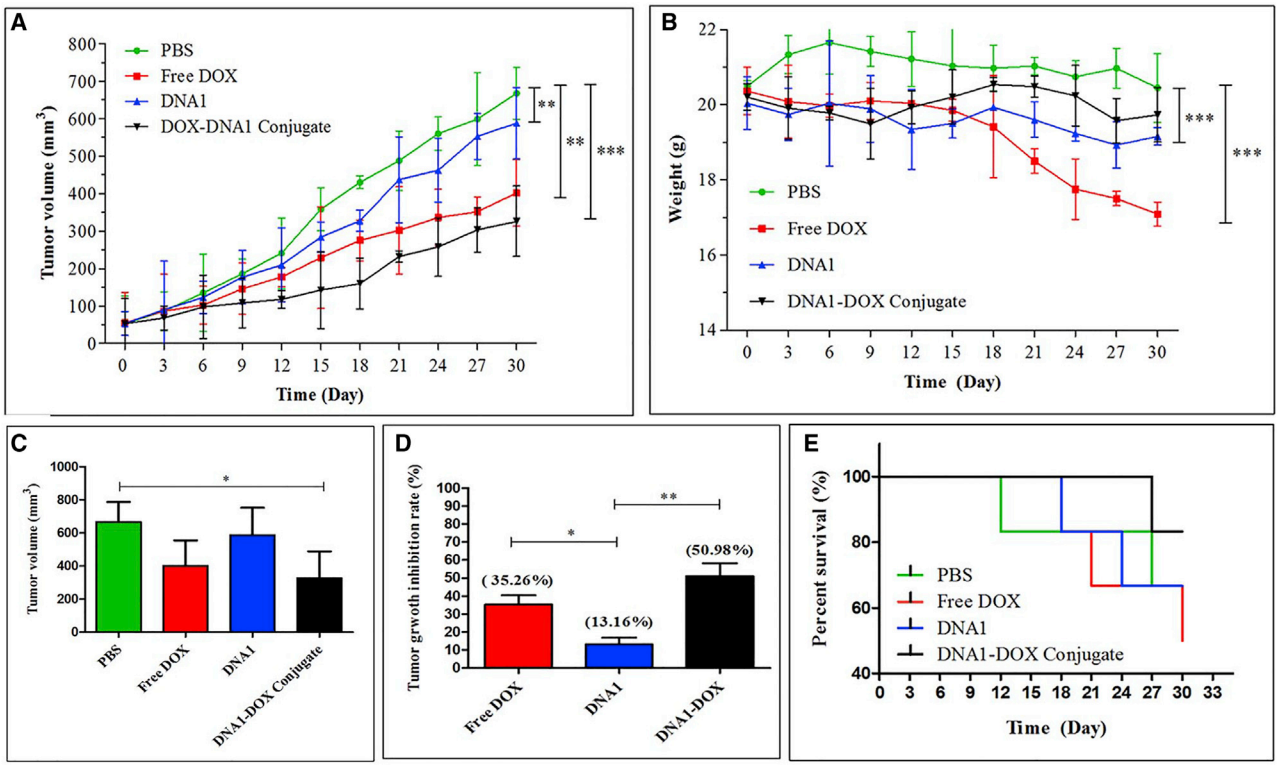

Figure 9. *In Vivo* Anti-Tumor Efficacy Study of Free DOX, DNA1 Aptamer, and DNA1-DOX Conjugate in BALB/C Nude Mice Injected s.c.
With A549 lung cancer cells at a dose of 15-mg/kg doxorubicin equivalent administered on days 0, 3, 6, 9, 12, 15 days. (A–E) Tumor growth rate (A), body weight changes (B), tumor volume changes (C), tumor growth inhibition rate (TIR%) (D), and survival curve (E) were recorded. Data are expressed as mean ± SD, and *$p < 0.05$, **$p < 0.01$, and ***$p < 0.001$ was considered statistically significant, n = 6.

Flow Cytometry Assays

The binding affinity and specificity of the aptamer toward A549, HepG2, MCF7, U-87 MG, and L-02 were studied by incubating these cells with varying concentrations of FAM-tagged DNA aptamer at 37°C for 1 h. In the next step, cells were washed and resuspended in 300 μL assay buffer and analyzed by flow cytometry. BD Accuri system was used to determine the fluorescence intensity by counting 10,000 events. The non-specific binding was determined by computing the fluorescence intensity for the ANXA1 negative (MCF7, L-02) cell line. Furthermore, the same strategy was also used to study the knockdown of ANXA1 in HepG2 and A549 cells.

Fluorescence Microscopy Imaging

To further determine the binding affinity and specificity of DNA1 aptamer, we observed fluorescence images of A549, HepG2, MCF7, U-87 MG, and L-02 cell lines bound with FAM-tagged DNA1 aptamer by Leica DM 4000B fluorescence microscope. Each cell line was cultured in a culture dish for 24 h at 37°C in a humid atmosphere of 5% CO_2. Subsequently, the supernatant was removed and the cells were washed and incubated with 250 nM DNA aptamer in assay buffer for 30 min at 37°C. Then cells were washed twice with binding buffer before imaging.

siRNA Mediated ANXA1 Knockdown in HepG2 and A549

HepG2 and A549 (4×10^5) cells were seeded in 6-well plate and incubated overnight at 37°C. Cells were treated with siRNA (25 pmol) negative control (5′-TTCTCCGAACGTGTCACGT-3′) and ANXA1 (5′-ATTCTATCAGAAGATGTAT-3′; Sangon Biotech, Shanghai, China) along with Lipofectamine-2000 (Invitrogen; 7.5 μL/well) in Opti-MEM (Invitrogen) for 6 h. After 6 h siRNA-Lipofectamine complex was removed and cells were washed with 1× PBS and fresh complete medium was replaced and cells were incubated for 48–72 h.

Gene knockdown efficiency was confirmed from mRNA levels of ANXA1 gene using qRT-PCR. Total RNA was extracted from Direct-zolTM RNA MiniPrep (Zymo Research, catalog number R2052) according to the manufacturer's instructions. cDNAs were synthesized from approximately 1 μg RNA with Prime Script RT Master Mix kit (Takara, Japan; Table 1). cDNAs were used for PCR amplification using SYBR Premix Ex Taq (Takara, Japan) according to the manufacturer's instructions on ABI Prism 7500 Sequence Detection System (Applied Biosystems, CA, USA) under the following conditions: 37°C for 15 min, 85°C for 5 s followed by 40 cycles at 95°C for 30 s, 95°C for 5 s, 60°C for 34 s, 95°C for 15 s, 60°C for 1 min, and 95°C for 15 s. Glyceraldehyde 3-phosphate dehydrogenase

Table 1. Sequence of Primer Used in qRT-PCR

AnnexinA1	Forward	5′-AGC GTC AAC AGA TCA AAG CAG CAT-3′
	Reverse	5′-AGA CCC TGT TAA TGT CTC TGA TTT-3′
GAPDH	Forward	5′-CCA TCA CCA TCT TCC AGGAG-3′
	Reverse	5′-CCT GCT TCA CCA CGT TCTTG-3′

(GAPDH) was amplified as an internal control. Data were analyzed using the comparative quantification cycle method (2-$^{\Delta\Delta}$Ct) (Table 1).

DOX Intercalation in DNA1 Aptamer

A physical conjugate between DNA1 aptamer and DOX was prepared by adding 1:75 molar ratio of DNA1 aptamer to DOX in conjugation buffer containing 5 mM $MgCl_2$, 0.05 M NaCl, pH 7.4, and incubated at 37°C for 1 h. To separate the DNA1 apt-DOX from free DOX, we then passed the conjugate mixture through Sephadex G-10 medium column of Sigma-Aldrich. 30 μL of DNA1 apt-DOX conjugate was added into acetonitrile (90 μL) and was vortexed for 1 min, followed by 5-min of centrifugation at 21,000 × *g*. The 50 μL of supernatant was diluted in 150 μL of buffer and was again subjected to 5 min of centrifugation at 21,000 × *g*. DOX quantification was done by measuring the natural fluorescence of DOX and its consequent quenching after intercalation. Fluorescence intensity of different DNA1 aptamer to DOX molar ratio in solution (0, 0.01, 0.03, 0.1, 0.3, 0.5, 1, 2, 3) were measured at excitation of 480 nm and emission of 500–700 nm. The DNA1 aptamer-DOX complex was freshly prepared before the experiment.

Cell Cytotoxicity Study using MTT

Cell viability was evaluated using MTT assay. ANXA1-positive (A549) and ANXA1-negative (MCF7) cells were seeded into 96-well plates, and RPMI-1640 medium supplemented with 10% FBS and 1% penicillin-streptomycin solution were used to culture the cells at 37°C. DOX with variable dose concentration were prepared in RPMI medium containing 10% FBS. Cells were then incubated with different treatment groups at 0.25, 0.5, 1, 2, 5, 10, 20, and 30 mg/mL of DOX equivalent concentration. After incubating the cells with the treatment group for 24 h, 20 μL of 5 mg/mL MTT solution was added to each well and incubated further for another 4 h at 37°C. Then medium containing MTT solution was discarded and 150 μL DMSO was added to each well to dissolve the formazan crystals. Finally, the assay to check the absorbance of soluble crystals was performed and recorded at 570 nm using a microplate reader. IC_{50} of the drug in the different formulation groups were calculated using GraphPad Prism.

Aptamer-Mediated Intracellular Targeting

Cellular internalization of free DOX and DNA1-D0X conjugate was assessed through confocal imaging in A549 cells. In brief, the cells were first seeded for 24 h to reach 80%–90% confluence before starting the experiment. After that, the cells were incubated with either free DOX or DNA1-DOX (1.5 μmol/L DOX concentration) for 12 h at 37°C. After 2 h and 12 h incubation, cells were washed three times with PBS, then the fresh medium was added, and the samples were placed for imaging by confocal microscopy. Fluorescence intensity of DOX in live cells was observed by confocal microscope at 488 nm as excitation wavelength in triplicate.

Anti-Tumor/Therapeutic Efficacy Study

BALB/c nude mice were injected subcutaneously in the right flank with 100 μL suspension of 1×10^5 A549 cells. After tumor size reached 50–60 mm,[3] the mice were divided into four (n = 6) treatment groups such as PBS, free DOX, DNA1, and DNA1-DOX Conjugate. The mice were treated with 6 consecutive doses on days 1, 3, 6, 9, 12, and 15 at 15 mg/kg doxorubicin equivalent dose. After 30 days, the tumor volume of the different treatment group was assessed. % TIR was calculated using the following formula:

$$\left(1 - \frac{TVt}{TVc}\right) \times 100$$

Here, TV_t and TV_c are the mean tumor volume of the treated and the control group, respectively. To understand the possibility of systemic toxicity of treatment groups, we analyzed body weight changes and the survival rate of different groups throughout the experiment period.

SUPPLEMENTAL INFORMATION

Supplemental Information can be found online at https://doi.org/10.1016/j.omtn.2020.07.038.

AUTHOR CONTRIBUTIONS

R. Bavi, K.K., B.-H.J., and Y.G. designed and supervised the study. R. Bavi, Z.H., P.B., M.A., M.J., and N.R. performed the experiments and analyzed the data. R. Bavi, P.B., S.B., and R. Bhosale wrote the paper. All authors reviewed and approved the final manuscript.

CONFLICTS OF INTEREST

The authors declare no competing interests.

ACKNOWLEDGMENTS

This work was supported by the Mid-Career Researcher Program of National Research Foundation of Korea(NRF), Ministry of Education, Science, and Technology (MEST) of the South Korean government (no. 2020R1A2C3004237). We also acknowledge financial support from the National Natural Science Foundation of China (NSFC 81220108012, 61335007, 81371684, 81000666, 81171395, 81328012, and 81729002). R. Bavi and N.R. are thankful to the University Grants Commission for Dr. D. S. Kothari postdoctoral fellowship.

REFERENCES

1. Raynal, P., and Pollard, H.B. (1994). Annexins: the problem of assessing the biological role for a gene family of multifunctional calcium- and phospholipid-binding proteins. Biochim. Biophys. Acta *1197*, 63–93.

2. Parente, L., and Solito, E. (2004). Annexin 1: more than an anti-phospholipase protein. Inflamm. Res. *53*, 125–132.

3. Pin, A.L., Houle, F., Fournier, P., Guillonneau, M., Paquet, E.R., Simard, M.J., Royal, I., and Huot, J. (2012). Annexin-1-mediated endothelial cell migration and angiogenesis are regulated by vascular endothelial growth factor (VEGF)-induced inhibition of miR-196a expression. J. Biol. Chem. *287*, 30541–30551.

4. Lim, L.H., and Pervaiz, S. (2007). Annexin 1: the new face of an old molecule. FASEB J. *21*, 968–975.

5. Padden, J., Ahrens, M., Kälsch, J., Bertram, S., Megger, D.A., Bracht, T., Eisenacher, M., Kocabayoglu, P., Meyer, H.E., Sipos, B., et al. (2016). Immunohistochemical Markers Distinguishing Cholangiocellular Carcinoma (CCC) from Pancreatic Ductal Adenocarcinoma (PDAC) Discovered by Proteomic Analysis of Microdissected Cells. Mol. Cell. Proteomics *15*, 1072–1082.

6. Hongsrichan, N., Rucksaken, R., Chamgramol, Y., Pinlaor, P., Techasen, A., Yongvanit, P., Khuntikeo, N., Pairojkul, C., and Pinlaor, S. (2013). Annexin A1: A new immunohistological marker of cholangiocarcinoma. World J. Gastroenterol. *19*, 2456–2465.

7. Falini, B., Tiacci, E., Liso, A., Basso, K., Sabattini, E., Pacini, R., Foa, R., Pulsoni, A., Dalla Favera, R., and Pileri, S. (2004). Simple diagnostic assay for hairy cell leukaemia by immunocytochemical detection of annexin A1 (ANXA1). Lancet *363*, 1869–1870.

8. Cheng, T.Y., Wu, M.S., Lin, J.T., Lin, M.T., Shun, C.T., Huang, H.Y., Hua, K.T., and Kuo, M.L. (2012). Annexin A1 is associated with gastric cancer survival and promotes gastric cancer cell invasiveness through the formyl peptide receptor/extracellular signal-regulated kinase/integrin beta-1-binding protein 1 pathway. Cancer *118*, 5757–5767.

9. Sato, Y., Kumamoto, K., Saito, K., Okayama, H., Hayase, S., Kofunato, Y., Miyamoto, K., Nakamura, I., Ohki, S., Koyama, Y., and Takenoshita, S. (2011). Up-regulated Annexin A1 expression in gastrointestinal cancer is associated with cancer invasion and lymph node metastasis. Exp. Ther. Med. *2*, 239–243.

10. Zhang, Z.Q., Li, X.J., Liu, G.T., Xia, Y., Zhang, X.Y., and Wen, H. (2013). Identification of Annexin A1 protein expression in human gastric adenocarcinoma using proteomics and tissue microarray. World J. Gastroenterol. *19*, 7795–7803.

11. Lin, Y., Lin, G., Fang, W., Zhu, H., and Chu, K. (2014). Increased expression of annexin A1 predicts poor prognosis in human hepatocellular carcinoma and enhances cell malignant phenotype. Med. Oncol. *31*, 327.

12. Biaoxue, R., Xiling, J., Shuanying, Y., Wei, Z., Xiguang, C., Jinsui, W., and Min, Z. (2012). Upregulation of Hsp90-beta and annexin A1 correlates with poor survival and lymphatic metastasis in lung cancer patients. J. Exp. Clin. Cancer Res. *31*, 70.

13. Boudhraa, Z., Rondepierre, F., Ouchchane, L., Kintossou, R., Trzeciakiewicz, A., Franck, F., Kanitakis, J., Labeille, B., Joubert-Zakeyh, J., Bouchon, B., et al. (2014). Annexin A1 in primary tumors promotes melanoma dissemination. Clin. Exp. Metastasis *31*, 749–760.

14. Bai, X.F., Ni, X.G., Zhao, P., Liu, S.M., Wang, H.X., Guo, B., Zhou, L.P., Liu, F., Zhang, J.S., Wang, K., et al. (2004). Overexpression of annexin 1 in pancreatic cancer and its clinical significance. World J. Gastroenterol. *10*, 1466–1470.

15. Paweletz, C.P., Ornstein, D.K., Roth, M.J., Bichsel, V.E., Gillespie, J.W., Calvert, V.S., Vocke, C.D., Hewitt, S.M., Duray, P.H., Herring, J., et al. (2000). Loss of annexin 1 correlates with early onset of tumorigenesis in esophageal and prostate carcinoma. Cancer Res. *60*, 6293–6297.

16. Garcia Pedrero, J.M., Fernandez, M.P., Morgan, R.O., Herrero Zapatero, A., Gonzalez, M.V., Suarez Nieto, C., and Rodrigo, J.P. (2004). Annexin A1 down-regulation in head and neck cancer is associated with epithelial differentiation status. Am. J. Pathol. *164*, 73–79.

17. Patton, K.T., Chen, H.M., Joseph, L., and Yang, X.J. (2005). Decreased annexin I expression in prostatic adenocarcinoma and in high-grade prostatic intraepithelial neoplasia. Histopathology *47*, 597–601.

18. Rodrigo, J.P., Garcia-Pedrero, J.M., Fernandez, M.P., Morgan, R.O., Suárez, C., and Herrero, A. (2005). Annexin A1 expression in nasopharyngeal carcinoma correlates with squamous differentiation. Am. J. Rhinol. *19*, 483–487.

19. Zhang, L., Yang, X., Zhong, L.P., Zhou, X.J., Pan, H.Y., Wei, K.J., Li, J., Chen, W.T., and Zhang, Z.Y. (2009). Decreased expression of Annexin A1 correlates with pathologic differentiation grade in oral squamous cell carcinoma. J. Oral Pathol. Med. *38*, 362–370.

20. Chen, X., Fan, Z., Chen, Y., Fang, X., and Sha, X. (2013). Retro-inverso carbohydrate mimetic peptides with annexin1-binding selectivity, are stable in vivo, and target tumor vasculature. PLoS ONE *8*, e80390.

21. Hatakeyama, S., Sugihara, K., Shibata, T.K., Nakayama, J., Akama, T.O., Tamura, N., Wong, S.M., Bobkov, A.A., Takano, Y., Ohyama, C., et al. (2011). Targeted drug delivery to tumor vasculature by a carbohydrate mimetic peptide. Proc. Natl. Acad. Sci. USA *108*, 19587–19592.

22. Pfeiffer, F., and Mayer, G. (2016). Selection and Biosensor Application of Aptamers for Small Molecules. Front Chem. *4*, 25.

23. Sefah, K., Shangguan, D., Xiong, X., O'Donoghue, M.B., and Tan, W. (2010). Development of DNA aptamers using Cell-SELEX. Nat. Protoc. *5*, 1169–1185.

24. Liang, H., Zhang, X.B., Lv, Y., Gong, L., Wang, R., Zhu, X., Yang, R., and Tan, W. (2014). Functional DNA-containing nanomaterials: cellular applications in biosensing, imaging, and targeted therapy. Acc. Chem. Res. *47*, 1891–1901.

25. Tuerk, C., and Gold, L. (1990). Systematic evolution of ligands by exponential enrichment: RNA ligands to bacteriophage T4 DNA polymerase. Science *249*, 505–510.

26. Osborne, S.E., and Ellington, A.D. (1997). Nucleic Acid Selection and the Challenge of Combinatorial Chemistry. Chem. Rev. *97*, 349–370.

27. Shcherbinin, D.S., Gnedenko, O.V., Khmeleva, S.A., Usanov, S.A., Gilep, A.A., Yantsevich, A.V., Shkel, T.V., Yushkevich, I.V., Radko, S.P., Ivanov, A.S., et al. (2015). Computer-aided design of aptamers for cytochrome p450. J. Struct. Biol. *191*, 112–119.

28. Chushak, Y., and Stone, M.O. (2009). In silico selection of RNA aptamers. Nucleic Acids Res. *37*, e87.

29. Weng, X., Luecke, H., Song, I.S., Kang, D.S., Kim, S.H., and Huber, R. (1993). Crystal structure of human annexin I at 2.5 A resolution. Protein Sci. *2*, 448–458.

30. Bavi, R., Kumar, R., Rampogu, S., Son, M., Park, C., Baek, A., Kim, H.H., Suh, J.K., Park, S.J., and Lee, K.W. (2016). Molecular interactions of UvrB protein and DNA from Helicobacter pylori: Insight into a molecular modeling approach. Comput. Biol. Med. *75*, 181–189.

31. Bavi, R., Kumar, R., Choi, L., and Woo Lee, K. (2016). Exploration of Novel Inhibitors for Bruton's Tyrosine Kinase by 3D QSAR Modeling and Molecular Dynamics Simulation. PLoS ONE *11*, e0147190.

32. Bavi, R., Kumar, R., Rampogu, S., Kim, Y., Kwon, Y.J., Park, S.J., and Lee, K.W. (2017). Novel virtual lead identification in the discovery of hematopoietic cell kinase (HCK) inhibitors: application of 3D QSAR and molecular dynamics simulation. J. Recept. Signal Transduct. Res. *37*, 224–238.

33. Kumar, R., Bavi, R., Jo, M.G., Arulalapperumal, V., Baek, A., Rampogu, S., Kim, M.O., and Lee, K.W. (2017). New compounds identified through in silico approaches reduce the α-synuclein expression by inhibiting prolyl oligopeptidase in vitro. Sci. Rep. *7*, 10827.

34. Kumar, R., Parameswaran, S., Bavi, R., Baek, A., Son, M., Rampogu, S., Park, C., Lee, G., Zeb, A., Parate, S., et al. (2019). Investigation of novel chemical scaffolds targeting prolyl oligopeptidase for neurological therapeutics. J. Mol. Graph. Model. *88*, 92–103.

35. Chaires, J.B., Herrera, J.E., and Waring, M.J. (1990). Preferential binding of daunomycin to 5'ATCG and 5'ATGC sequences revealed by footprinting titration experiments. Biochemistry *29*, 6145–6153.

36. Zadeh, J.N., Steenberg, C.D., Bois, J.S., Wolfe, B.R., Pierce, M.B., Khan, A.R., Dirks, R.M., and Pierce, N.A. (2011). NUPACK: Analysis and design of nucleic acid systems. J. Comput. Chem. *32*, 170–173.

37. Hu, Y., Duan, J., Zhan, Q., Wang, F., Lu, X., and Yang, X.D. (2012). Novel MUC1 aptamer selectively delivers cytotoxic agent to cancer cells in vitro. PLoS ONE *7*, e31970.

38. Shcherbinin, D.S., and Veselovslĭ, A.V. (2013). [Investigation of interaction of thrombin-binding aptamer with thrombin and prethrombin-2 by simulation of molecular dynamics]. Biofizika *58*, 415–424.

39. Baldrich, E., and Zourob, M. (2010). Aptamers: versatile tools for reagentless aptasensing. In Recognition Receptors in Biosensors (Springer), pp. 675–772.

40. Yao, F., An, Y., Li, X., Li, Z., Duan, J., and Yang, X.D. (2020). Targeted Therapy of Colon Cancer by Aptamer-Guided Holliday Junctions Loaded with Doxorubicin. Int. J. Nanomedicine *15*, 2119–2129.

41. Ellingson, S.R., Smith, J.C., and Baudry, J. (2013). VinaMPI: facilitating multiple receptor high-throughput virtual docking on high-performance computers. J. Comput. Chem. *34*, 2212–2221.

42. Aliev, A.E., Kulke, M., Khaneja, H.S., Chudasama, V., Sheppard, T.D., and Lanigan, R.M. (2014). Motional timescale predictions by molecular dynamics simulations: case study using proline and hydroxyproline sidechain dynamics. Proteins *82*, 195–215.

43. Bavi, R., Liu, Z., Han, Z., Zhang, H., and Gu, Y. (2019). In silico designed RNA aptamer against epithelial cell adhesion molecule for cancer cell imaging. Biochem. Biophys. Res. Commun. *509*, 937–942.

44. Pérez, A., Marchán, I., Svozil, D., Sponer, J., Cheatham, T.E., 3rd, Laughton, C.A., and Orozco, M. (2007). Refinement of the AMBER force field for nucleic acids: improving the description of alpha/gamma conformers. Biophys. J. *92*, 3817–3829.

45. Hess, B., Bekker, H., Berendsen, H.J.C., and Fraaije, J.G.E.M. (1997). LINCS: a linear constraint solver for molecular simulations. J. Comput. Chem. *18*, 1463–1472.

46. Essmann, U., Perera, L., and Berkowitzet, M.L. (1995). A smooth particle mesh Ewald method. J. Chem. Phys. *15*, 8577–8593.